diabetes
American Diabetes Association

MAD2-Dependent Insulin Receptor Endocytosis Regulates Metabolic Homeostasis

Junhee Park, Catherine Hall, Brandon Hubbard, Traci LaMoia, Rafael Gaspar, Ali Nasiri, Fang Li, Hanrui Zhang, Jiyeon Kim, Rebecca A. Haeusler, Domenico Accili, Gerald I. Shulman, Hongtao Yu, and Eunhee Choi

Diabetes 2023;72(12):1781–1794 | https://doi.org/10.2337/db23-0314

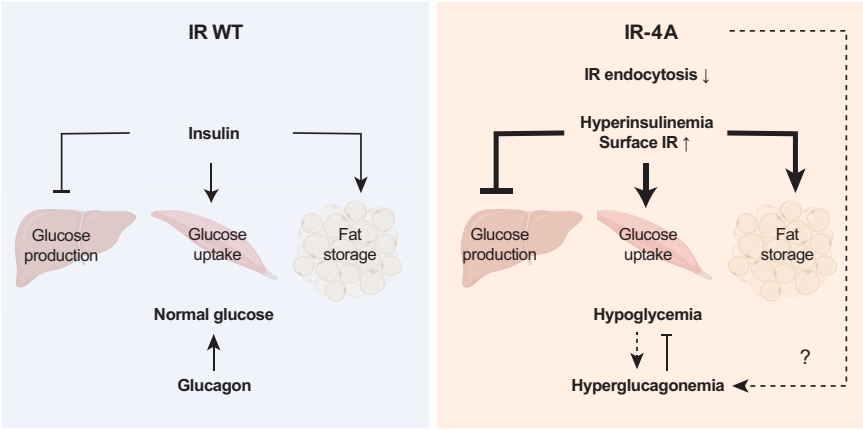

IR, insulin receptor; WT, wild type.

MAD2-Dependent Insulin Receptor Endocytosis Regulates Metabolic Homeostasis

Junhee Park,[1] Catherine Hall,[1] Brandon Hubbard,[2] Traci LaMoia,[2] Rafael Gaspar,[2] Ali Nasiri,[2] Fang Li,[3] Hanrui Zhang,[3] Jiyeon Kim,[4] Rebecca A. Haeusler,[1,5,6] Domenico Accili,[5,6] Gerald I. Shulman,[2] Hongtao Yu,[7] and Eunhee Choi[1]

Diabetes 2023;72:1781–1794 | https://doi.org/10.2337/db23-0314

Insulin activates insulin receptor (IR) signaling and subsequently triggers IR endocytosis to attenuate signaling. Cell division regulators MAD2, BUBR1, and p31^{comet} promote IR endocytosis on insulin stimulation. Here, we show that genetic ablation of the IR-MAD2 interaction in mice delays IR endocytosis, increases IR levels, and prolongs insulin action at the cell surface. This in turn causes a defect in insulin clearance and increases circulating insulin levels, unexpectedly increasing glucagon levels, which alters glucose metabolism modestly. Disruption of the IR-MAD2 interaction increases serum fatty acid concentrations and hepatic fat accumulation in fasted male mice. Furthermore, disruption of the IR-MAD2 interaction distinctly changes metabolic and transcriptomic profiles in the liver and adipose tissues. Our findings establish the function of cell division regulators in insulin signaling and provide insights into the metabolic functions of IR endocytosis.

ARTICLE HIGHLIGHTS

- The physiological role of IR endocytosis in insulin sensitivity remains unclear.
- Disruption of the IR-MAD2 interaction delays IR endocytosis and prolongs insulin signaling.
- IR-MAD2 controls insulin clearance and glucose metabolism.
- IR-MAD2 maintains energy homeostasis.

Insulin binds to and activates insulin receptor (IR), a receptor tyrosine kinase (1–6). Insulin-stimulated IR triggers two distinct signaling cascades: the phosphatidylinositol 3-kinase (PI3K)-AKT pathway and the mitogen-activated protein kinase (MAPK) pathway. These two pathways maintain glucose, lipid, and amino acid homeostasis and regulate cell growth and proliferation (4,7–9). Insulin-activated IR undergoes endocytosis and is either recycled to the cell surface to initiate a new round of insulin signaling or degraded in the lysosome (10–13) (Fig. 1*A*). Perturbations of insulin signaling cause metabolic disorders, such as diabetes and severe insulin resistance syndromes (4,8,14).

IR endocytosis, particularly in the liver, facilitates insulin clearance from portal circulation (15,16). Therefore, in addition to insulin secretion by pancreatic β-cells, hepatic insulin clearance by IR endocytosis plays a crucial role in maintaining proper insulin levels and its action in peripheral insulin-target tissues (15). Hepatic IR knockout (KO) or carcinoembryonic antigen-related cell adhesion molecule 1 (CEACAM1) KO mice exhibited defects in IR endocytosis, leading to hyperinsulinemia and systemic insulin resistance (17–19). Conversely, hepatic inhibition of EPH receptor B4 (EPHB4)-dependent IR endocytosis and lysosomal degradation improved insulin and glucose tolerance in obese mice (20). Furthermore, inhibition of INCEPTOR

[1]Department of Pathology and Cell Biology, Vagelos College of Physicians and Surgeons, Columbia University, New York, NY
[2]Departments of Internal Medicine and Cellular and Molecular Physiology, Yale School of Medicine, New Haven, CT
[3]Cardiometabolic Genomics Program, Division of Cardiology, Department of Medicine, Columbia University Irving Medical Center, New York, NY
[4]Department of Urology and Department of Cellular and Molecular Physiology, Yale School of Medicine, New Haven, CT
[5]Naomi Berrie Diabetes Center, Columbia University, New York, NY
[6]Department of Medicine, Vagelos College of Physicians and Surgeons, Columbia University, New York, NY
[7]School of Life Sciences, Westlake University, Hangzhou, Zhejiang Province, China

Corresponding author: Eunhee Choi, EC3477@cumc.columbia.edu

Received 24 April 2023 and accepted 12 September 2023

This article contains supplementary material online at https://doi.org/10.2337/figshare.24147744.

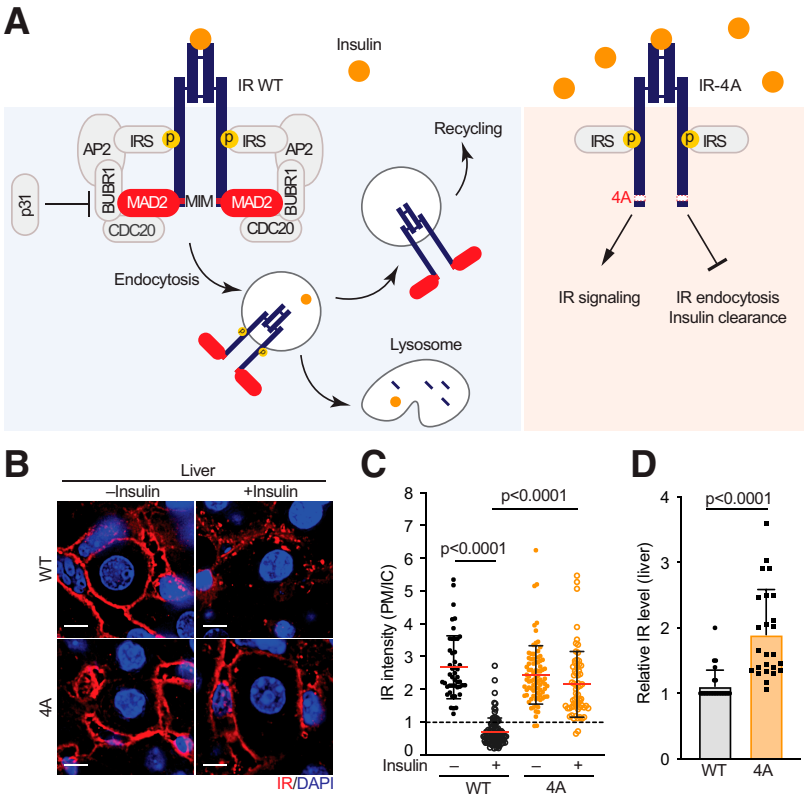

Figure 1—MAD2 is required for insulin-activated IR endocytosis. *A*: Schematic illustration of IR-MAD2 interaction (left) and IR-4A mutant (right). *B*: Liver sections of WT and IR-4A mice injected with PBS (−insulin) or insulin (+insulin) were stained with anti-IR (red) antibodies and DAPI (blue). Scale bar, 10 μm. *C*: Quantification of the ratios of PM and intracellular compartment (IC) IR signals of the livers in *B*. Mean ± SD, $N = 3$ mice each. Significance calculated with two-tailed Student *t* test. *D*: Relative IR levels of whole-liver lysates of WT and IR-4A mice. Mean ± SD. $N = 25$ mice each. Significance calculated with two-tailed Student *t* test. $P < 0.0001$. 4A, IR-4A; IRS, insulin receptor substrate.

(insulin inhibitory receptor) enhanced insulin signaling in β-cells and improved glucose tolerance (21). We previously showed that accelerated IR endocytosis in liver caused whole-body insulin resistance (22), whereas delayed IR endocytosis in the liver by Src homology phosphatase 2 (SHP2) inhibition prolonged insulin signaling and increased insulin sensitivity in mice (23). Our findings support the idea that IR endocytosis terminates and redistributes insulin signaling. At present, the function of IR endocytosis in whole-body insulin sensitivity is not well understood. It is unclear whether the metabolic phenotypes described above depend solely on IR endocytosis or on other IR functions, such as the IR kinase activity, or even IR-independent functions.

Cell division regulators MAD2, BUBR1, and $p31^{comet}$ regulate IR endocytosis and signaling (10,22,23). Mitosis arrest deficiency 2 (MAD2) directly binds to IR through the MAD2-interacting motif (MIM) in the COOH terminus of IR and collaborates with budding uninhibited by benomyl 1–related 1 (BUBR1) to recruit clathrin adaptor protein AP2 to IR (Fig. 1*A*). $p31^{comet}$ inhibits the association of BUBR1-AP2 to IR, thereby preventing IR endocytosis. Here, we report that genetic ablation of the MIM of IR delays IR endocytosis and prolongs insulin action at the cell surface, while simultaneously increasing insulin and glucose counterregulatory factors and altering whole-body metabolic homeostasis. Our results demonstrate the importance of IR endocytosis in metabolic regulation.

RESEARCH DESIGN AND METHODS

Mice

Animal work described in this article was approved and conducted under the oversight of the Columbia University Institutional Animal Care and Use Committee. Mice were fed a standard rodent chow (no. 5053; LabDiet) or high-fat diet (HFD) (D12492; Research Diets) for indicated periods. All animals were maintained in a specific antigen-free barrier facility with 12-h light/dark cycles (6:00 A.M. on and 6:00 P.M. off). Two- to three-month-old male mice were used in this study unless otherwise noted. For inducing insulin resistance, mice were fed an HFD (60%) (D12492; Research Diets). Gene targeting strategies, hyperinsulinemic-euglycemic clamp, and metabolic cage studies are described in Supplementary Material.

Insulin Signaling and IR Endocytosis In Vivo

Insulin signaling and IR endocytosis in vivo analyses were performed as previously described with some modifications (22–24). Male mice 2–3 months old were fasted overnight. Following anesthesia, mice were injected with 6 nmol Humulin

(Eli Lilly) per mouse via inferior vena cava. Livers were removed at 3 min after injection. Adipose tissues and skeletal muscle were removed at 5 min and 7 min after injection, respectively. Hypothalamus was collected at 10 min after 30 nmol/mouse Humulin injection via inferior vena cava. Adipose tissues were homogenized in radioimmunoprecipitation assay buffer (50 mmol/L Tris [pH 8.0], 150 mmol/L NaCl, 1% [v/v] NP-40, 0.5% [w/v] sodium deoxycholate, 0.1% [w/v] SDS, and 1 mmol/L EDTA), and other tissues were mixed with lysis buffer B (50 mmol/L HEPES, 150 mmol/L NaCl, 10% [v/v] glycerol, 1% [v/v] triton X-100, 1 mmol/L EDTA, 0.5 mmol/L dithiothreitol, and 2 mmol/L phenylmethylsulfonyl fluoride) supplemented with cOmplete Protease Inhibitor Cocktail (Roche), PhosSTOP (Sigma-Aldrich), and 25 units/mL Turbo-Nuclease (Accelagen), homogenized with Fisherbrand Bead Mill homogenizer, and then incubated on ice for 1 h. After centrifuge at 20,817*g* at 4°C for 30 min, the concentrations of cell lysate were measured with Micro BCA Protein Assay Kit (Thermo Fisher Scientific). The lysates were then analyzed with quantitative Western blotting (LI-COR, Lincoln, NE). The antibodies used for this study are listed in Supplementary Table 1.

Primary Hepatocytes Isolation

Mouse primary hepatocytes were isolated from 2- to 3-month-old male mice with a standard two-step collagenase perfusion procedure as previously described (22,24). Isolated hepatocytes were resuspended with attached medium (Williams' Medium E supplemented with 10% [v/v] FBS, 100 pmol/L insulin, 100 nmol/L dexamethasone, 5.5 μg/mL transferrin, 6.7 ng/mL sodium selenite, and 1% penicillin/streptomycin) and plated on collagen (no. C3867; Sigma-Aldrich)-coated dishes. After 4 h, the medium was changed to serum-free low-glucose DMEM. After 14–16 h, the cells were treated with insulin for analysis of IR signaling.

Biochemical Measurements

For serum preparation, blood was centrifuged and stored at −80°C after forming clots at room temperature for 30 min. Serum insulin and C-peptide were measured with ultrasensitive mouse insulin ELISA kits (no. 90080; Crystal Chem) and mouse C-peptide ELISA kits (80-CPTMS-E01; ALPCO). Plasma samples were collected from facial vein bleeding with venous blood collection tubes (41.13950.105; Sarstedt). Plasma glucagon, noradrenaline, adrenaline, and fatty acids (FA) were measured with mouse glucagon ELISA kits (81518; Crystal Chem), Bi-CAT adrenaline and noradrenaline ELISA kits (17-BCTHU-E02-RES; ALPCO), and FA quantification colorimetric/fluorometric kits (ab65341; Abcam). Blood glucose and HbA_{1c} levels from tail bleeding were measured with a glucometer (AlphaTrak) and A1C Now+ (Bayer Vital) test kits. Plasma and hepatic triglyceride levels were measured with triglyceride quantification colorimetric/fluorometric kits (MAK266; Sigma-Aldrich).

Glucose, Insulin, and Pyruvate Tolerance Tests

For glucose tolerance tests, mice were fasted for 6 h and their blood glucose levels (T = 0) were measured with tail bleeding. Then glucose (2 g/kg body wt) was injected intraperitoneally or using oral gavage. Blood glucose levels were measured at indicated time points after glucose injection. For insulin tolerance tests (ITT), mice fasted for 2 h were injected intraperitoneally with Humulin (6 nmol/kg body wt). For pyruvate tolerance tests (PTT), mice fasted for 14 h were injected with pyruvate (1 g/kg body wt) (P5280; Sigma-Aldrich).

Tissue Diacylglycerols and PKCε Translocation Analyses

Hepatic diacylglycerols (DAGs) levels and PKCε translocation were analyzed as previously described (25). Briefly, DAGs were extracted from tissues with 2:1 chloroform:-methanol (v/v) with 0.01% butylated hydroxytoluene, dried down, and redissolved in 95:5:0.5 hexane/methylene chloride/ethyl ether (v/v/v) before analysis with liquid chromatography–tandem mass spectrometry.

Liver lysates with buffer A (20 mmol/L Tris-HCl, pH 7.4, 1 mmol/L EDTA, 0.25 mmol/L EGTA, 250 mmol/L sucrose, and freshly added protease and phosphatase inhibitors; Roche Diagnostics) were centrifuged (60 min, 100,000*g*, 4°C), and the supernatant was saved as the cytosolic fraction. The pellet was resuspended in buffer B (250 mmol/L Tris-HCl, pH 7.4, 1 mmol/L EDTA, 0.25 mmol/L EGTA, 2% Triton X-100, and freshly added protease and phosphatase inhibitors) and centrifuged (60 min, 100,000*g*, 4°C). An aliquot of the supernatant was saved as the membrane fraction. The resulting protein samples were subjected to Western blot analysis with anti-PKCε, anti–Na-K ATPase, and anti-GAPDH antibodies. After washing, membranes were incubated with horseradish peroxidase–conjugated secondary antibody (Cell Signaling Technology). Detection was performed with enhanced chemiluminescence.

Tissue Histology and Immunohistochemistry

Mouse tissues were fixed in buffered 10% neutral buffered formalin for hematoxylin-eosin (H-E) staining, oil red O staining, or periodic acid Schiff staining by Molecular Pathology Core at Columbia University. Stained slides were scanned with a Leica SCN400 scanner. For IR endocytosis assays, the livers were fixed in 10% neutral buffered formalin and embedded in paraffin blocks. Sections were deparaffinized, subjected to antigen retrieval with 10 mmol/L sodium citrate (pH 6.0), incubated with 0.3% H_2O_2, blocked with 0.3% BSA, and then incubated with anti-IR antibodies. The slides were counterstained with DAPI. Adipocyte sizes were assessed with Adiposoft software in ImageJ on scanned images of formalin-fixed adipose tissue.

Statistical Analysis

Prism 9 was used for the generation of graphs and for statistical analyses. Results are presented as mean ± SD or mean ± SEM. Two-tailed unpaired *t* tests were used for pairwise significance analysis. Two-way ANOVA followed

by Tukey multiple comparisons test was used. Sample sizes were determined based on the maximum number of mice. Power analysis for sample sizes was not performed. Randomization and blinding methods were not used, and data were analyzed after the completion of all data collection in each experiment.

Data and Resource Availability

All data are available in the main text or Supplementary Material. RNA-sequencing data are available in the Gene Expression Omnibus (GEO) (GSE240578).

RESULTS

Disruption of the IR-MAD2 Interaction Delays IR Endocytosis

We previously showed that the IR mutant with four residues in its MIM mutated to alanine (IR-4A) was deficient in MAD2 binding and insulin-induced IR endocytosis (10,22,23). To determine the physiological function of the IR-MAD2 interaction, we generated IR-4A knock-in (IR-4A) mice with CRISPR/Cas9 (Supplementary Fig. 1*A*). IR-4A mice survived and did not show discernable differences from wild-type (WT) mice. Metabolic cage analyses of male mice fed normal chow diet did not show significant effects on whole-body oxygen consumption, carbon dioxide production, respiratory quotient, energy expenditure, caloric intake, or activity in IR-4A mice compared with WT mice (Fig. 1*A* and Supplementary Fig. 2).

Insulin-activated IR is internalized, ultimately leading to downregulation of insulin signaling (26in vivo, overnight-fasted WT and IR-4A mice were injected with insulin via inferior vena cava. The livers were collected from these mice and subjected to analysis of localization of the endogenous IR. As expected, insulin treatment promoted IR internalization in the WT liver, whereas IR in IR-4A liver retained its plasma membrane (PM) localization (Fig. 1*B* and *C*). Consequently, the basal IR level in IR-4A mice was higher than that of WT mice (Fig. 1*D* and Supplementary Fig. 1*B–F*). These data establish the importance of the IR-MAD2 interaction in IR endocytosis and basal level of IR in vivo.

Next, we monitored the activating phosphorylation of IR (pY962 in the juxtamembrane region and pY1152/1153 in the kinase domain, with amino acid numbering for mature mouse IR-A isoform), and downstream phosphorylation events, including AKT and ERK1/2 in liver, skeletal muscle, and epididymal white adipose tissue (eWAT) (Fig. 2*A* and Supplementary Fig. 1*E* and *F*) on insulin stimulation. The levels of phosphorylated (p)IR and pAKT in IR-4A mice were slightly increased, as compared with WT mice. pERK levels were similar between the two groups. Consistent with in vivo findings, freshly isolated IR-4A primary hepatocytes showed slightly enhanced and extended pIR and pAKT at multiple time points and various insulin concentrations (Fig. 2*B–E*). No significant differences in pERK levels were observed between WT and IR-4A hepatocytes. Furthermore, the pIR and pAKT levels were mildly elevated in IR-4A in particular muscle under the refeeding condition (Supplementary Fig. 3*A* and *B*). These data suggest that disruption of the IR-MAD2 interaction delays IR endocytosis and degradation of IR/insulin complexes, marginally prolonging IR signaling.

IR-MAD2 Controls Insulin Clearance

IR endocytosis in liver plays an important role in insulin clearance. Liver-specific IR KO mice and CEACAM1 KO mice develop hyperinsulinemia (18,27). We thus examined the levels of insulin and a cleavage product of proinsulin, C-peptide. C-peptide level was not altered in IR-4A mice, suggesting that the IR-MAD2 interaction does not affect insulin secretion (Fig. 3*A*). In IR-4A mice, serum insulin level was significantly increased (Fig. 3*B*), thus lowering the C-peptide–to–insulin ratio (Fig. 3*C*). Hepatic CEACAM1 level was not altered by the IR-4A mutation (Supplementary Fig. 3*C* and *D*). These data suggest that disruption of the IR-MAD2 interaction delays insulin clearance, thus increasing peripheral insulin levels.

IR-4A mice displayed mild hypoglycemia possibly due to the high insulin levels, but no significant changes were observed after 6 h fasting (Fig. 3*D*). Plasma glucose concentrations are also regulated by glucose counterregulatory factors, such as glucagon and (nor)adrenaline, which increase glucose and FA in the bloodstream (28–30). In IR-4A mice fed normal chow diet, plasma glucagon and noradrenaline concentrations were increased (Fig. 3*E* and *F*), but not plasma adrenaline (Fig. 3*G*). These data suggest that glucose counterregulatory mechanisms are activated to maintain glucose homeostasis during chronic mild high-insulin and low-glucose conditions in IR-4A mice.

IR-MAD2 Maintains Glucose Homeostasis

To determine the function of IR-MAD2 in metabolic homeostasis, we monitored metabolic phenotypes under normal chow feeding in young (2- to 3-month-old) and old (13-month-old) WT and IR-4A mice. Young IR-4A mice exhibited improved glucose tolerance and mildly increased insulin levels compared with WT mice (Fig. 4*A–C*), suggesting that the increased insulin levels facilitate glucose clearance. Strikingly, there were no significant differences in ITT and PTT (Fig. 4*D–G*).

To directly assess the whole-body insulin sensitivity of young IR-4A mice, we performed hyperinsulinemic-euglycemic clamp studies. During the clamp analysis, plasma glucose levels are adjusted between the groups to reach ∼110 mg/mL (Fig. 4*H*). By experimental design, the high dose of insulin infusion during the clamp significantly increased insulin levels, and to a similar extent in WT and IR-4A mice (Fig. 4*I*). Although IR-4A mice have a slightly higher glucose infusion rate (Fig. 4*J* and *K*), they displayed suppression of endogenous glucose production (EGP) and plasma FA similar to that of WT mice (Fig. 4*L* and *M*). The insulin-stimulated glucose uptake was slightly, but not significantly, increased (Fig. 4*N*). These data suggest that, despite the prolonged IR signaling in IR-4A mice, the disruption of the IR-MAD2 interaction does not significantly enhance whole-body insulin sensitivity in young mice,

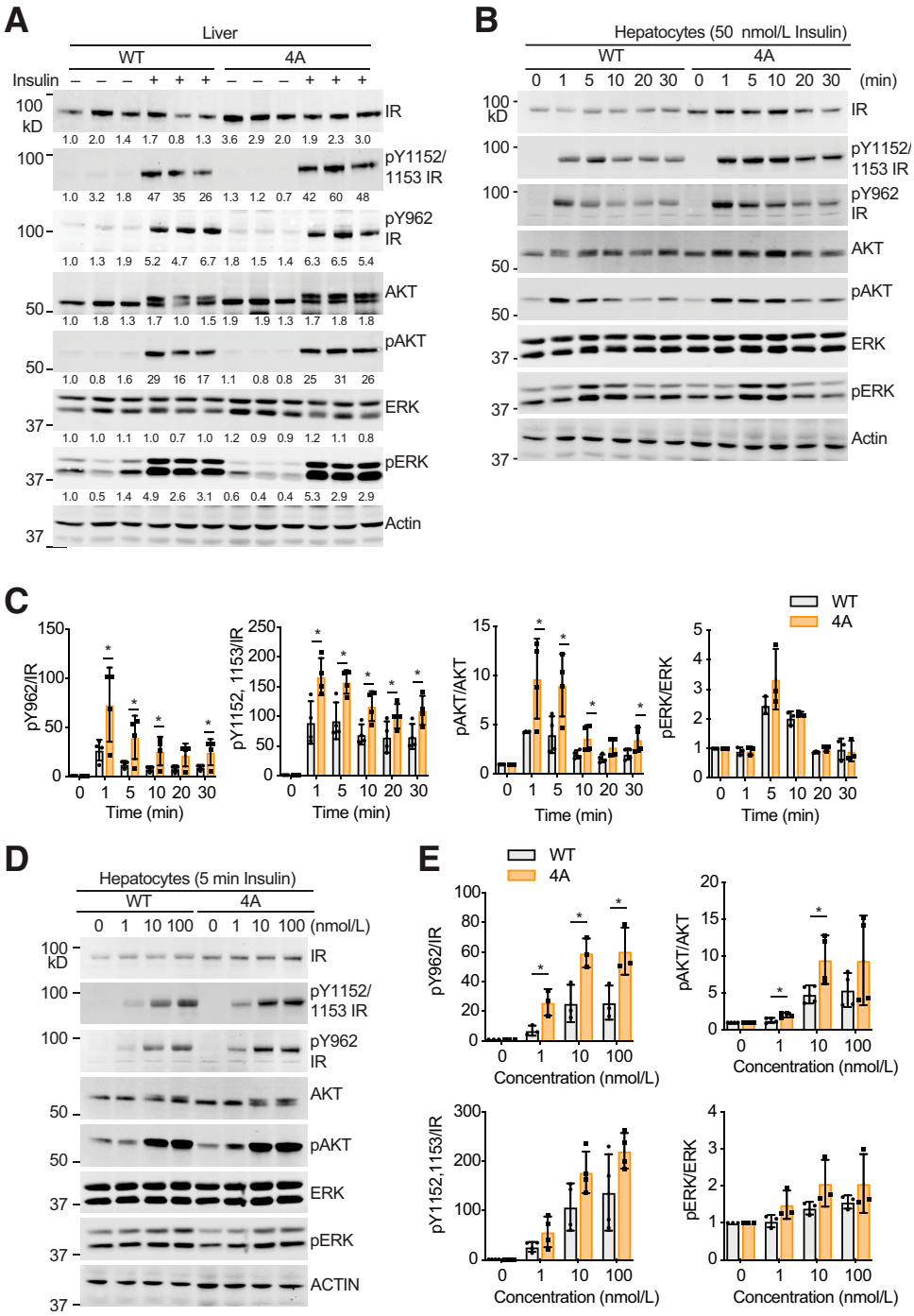

Figure 2—Disruption of IR-MAD2 interaction prolongs insulin signaling. *A*: IR signaling in whole-liver lysates of WT and IR-4A mice treated without (–) or with (+) insulin. Each lane contains lysate from an individual mouse. Below are the relative band intensities, normalized to Actin. *B*: IR signaling in primary WT and IR-4A hepatocytes treated with 50 nmol/L insulin for the indicated time points. *C*: Quantification of the Western blot data shown in *B*. Mean ± SD. pY1152, 1153/IR, pY962/IR, pAKT/AKT, $N = 4$; pERK/ERK, $N = 3$. Significance calculated with two-tailed Student *t* test; $*P < 0.05$. *D*: IR signaling in primary WT and IR-4A hepatocytes treated with the indicated concentrations of insulin for 10 min. *E*: Quantification of the Western blot data shown in *D*. Mean ± SD. pY1152, 1153/IR and pAKT/AKT, $N = 4$; pY962/IR and pERK/ERK, $N = 3$. Significance calculated with two-tailed Student *t* test; $*P < 0.05$. 4A, IR-4A.

possibly due to increased negative feedback pathways on mild but chronic hyperinsulinemia and hypoglycemia.

IR-4A mice were followed longitudinally for examination of the metabolic function of IR-MAD2 in aging mice. With aging, peripheral insulin resistance progressively increases and insulin clearance declines, resulting in elevation of circulating insulin levels (31–33). Consistently, aged WT mice exhibited increased serum insulin levels, while insulin levels for

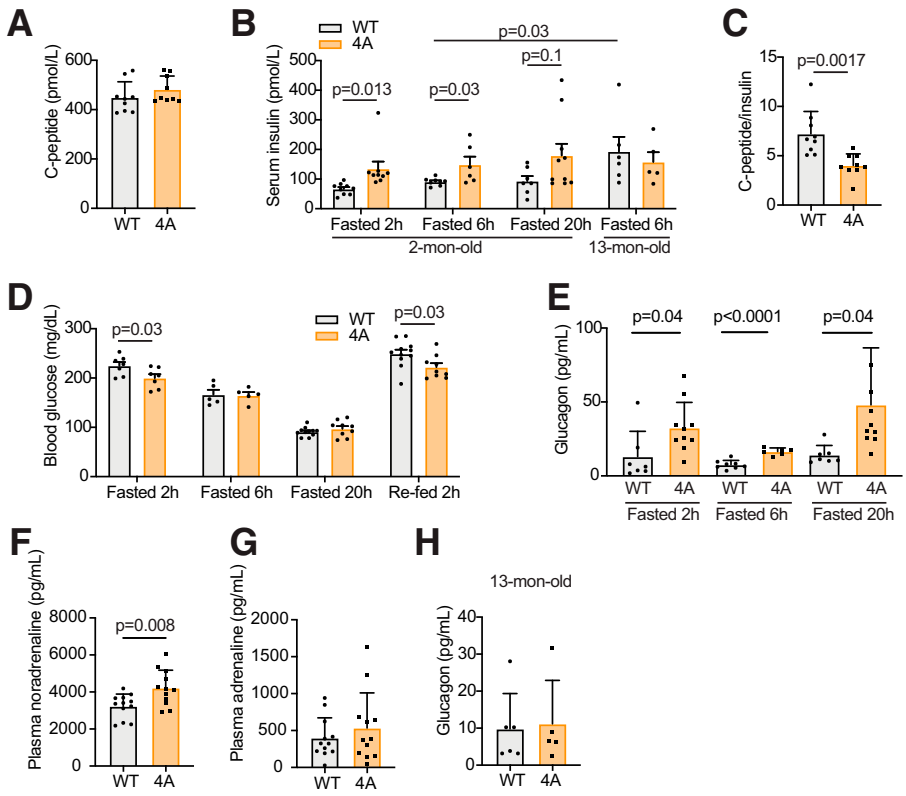

Figure 3—Disruption of IR-MAD2 interaction increases in circulating insulin levels and enhances glucose counterregulatory responses. *A*: Serum C-peptide level in 2- to 3-month-old male mice fasted for 6 h. Mean ± SD. *N* = 9 mice each. *B*: Serum insulin level in male mice. Mean ± SD. *N* = 9 mice each. Significance calculated with two-tailed Student *t* test. *C*: The ratio of C-peptide to insulin in 2- to 3-month-old male mice fasted for 6 h. Significance calculated with two-tailed Student *t* test. *D*: Blood glucose levels in 2- to 3-month-old male WT and IR-4A mice. Mean ± SD. WT, fasted 2 h, *N* = 7; IR-4A, fasted 2 h, *N* = 7; WT, fasted 6 h, *N* = 5; IR-4A, fasted 6 h, *N* = 5; WT, fasted 20 h, *N* = 11; IR-4A, fasted 20 h, *N* = 9; WT, refed 2 h, *N* = 11; IR-4A, refed 2 h, *N* = 9. Significance calculated with two-tailed Student *t* test. *E*: Plasma glucagon level in 2- to 3-month-old male mice fed normal chow diet. Mean ± SD. WT, fasted 2 h, *N* = 7; IR-4A, fasted 2 h, *N* = 10; WT, fasted 6 h, *N* = 8; IR-4A, fasted 6 h, *N* = 6; WT, fasted 20 h, *N* = 7; IR-4A, fasted 20 h, *N* = 10. Significance calculated with two-tailed Student *t* test. *F*: Plasma noradrenaline level in 2- to 3-month-old male mice fed normal chow diet. Mice were fasted for 6 h. Mean ± SD. *N* = 12 mice each. Significance calculated with two-tailed Student *t* test. *G*: Plasma adrenaline level in 2- to 3-month-old male mice fed normal chow diet. Mice were fasted for 6 h. Mean ± SD. *N* = 12 mice each. *H*: Plasma glucagon level in 13-month-old male mice fed normal chow diet. Mice were fasted for 6 h. WT, *N* = 6; IR-4A, *N* = 5. 4A, IR-4A; mon, month.

aged IR-4A mice did not further increase (Fig. 3*B*). Thus, the fact that insulin levels did not differ between young and old IR-4A mice suggests an acquired defect in insulin homeostasis in WT mice rather than a reversal of the IR internalization in IR-4A mice. There was no significant difference in glucagon levels (Fig. 3*H*) and glucose tolerance between old WT and IR-4A mice (Fig. 4*O* and *P*). Furthermore, unlike in young IR-4A mice, mild hypoglycemia was not observed in the IR-4A mice as they aged. Strikingly, ITT demonstrated that old IR-4A mice are more sensitive to insulin with respect to glucose clearance (Fig. 4*Q* and *R*). These data suggest that the disruption of IR-MAD2 interaction delays the onset of age-related insulin resistance, possibly by prolonging insulin signaling. The data further suggest that delayed IR endocytosis improves insulin sensitivity in vivo after high-dose insulin injection.

Next, we investigated the metabolic effects of HFD feeding on WT and IR-4A mice. In comparison with WT littermates, IR-4A mice had a trend toward increasing body weight (Fig. 5*A*). As expected, serum insulin levels in mice fed HFD were substantially higher than in those fed normal chow (Fig. 5*B*). Both WT and IR-4A mice showed a marked increase in serum insulin concentrations after 8 days of HFD feeding, and this increase continued over time (Fig. 5*B*). Insulin levels of IR-4A mice were similar to those of WT mice 8 days after HFD feeding (Fig. 5*B*), with modest hypoglycemia and virtually unchanged glucose tolerance (Fig. 5*E* and *F*). Interestingly, IR-4A mice fed HFD for 8 days exhibited increased insulin sensitivity during an ITT (Fig. 5*G* and *H*). In contrast, IR-4A mice fed HFD for 11 weeks exhibited decreased fasting serum glucose levels (Fig. 5*C* and *D* and Supplementary Fig. 3*E*) but did not show increased glucose or insulin sensitivity (Fig. 5*I*–*L*). These results suggest that the disruption of the IR-MAD2 interaction delays the development of short-term diet-induced insulin resistance but cannot prevent prolonged diet-induced metabolic complications.

IR-MAD2 Maintains Energy Homeostasis

Fasting promotes hydrolysis of triacylglycerols (TG) in adipose tissues and increases circulating FA (34,35). FA are taken up by the liver, where they are esterified to TG or oxidized by β-oxidation into acetyl-CoA, which is then

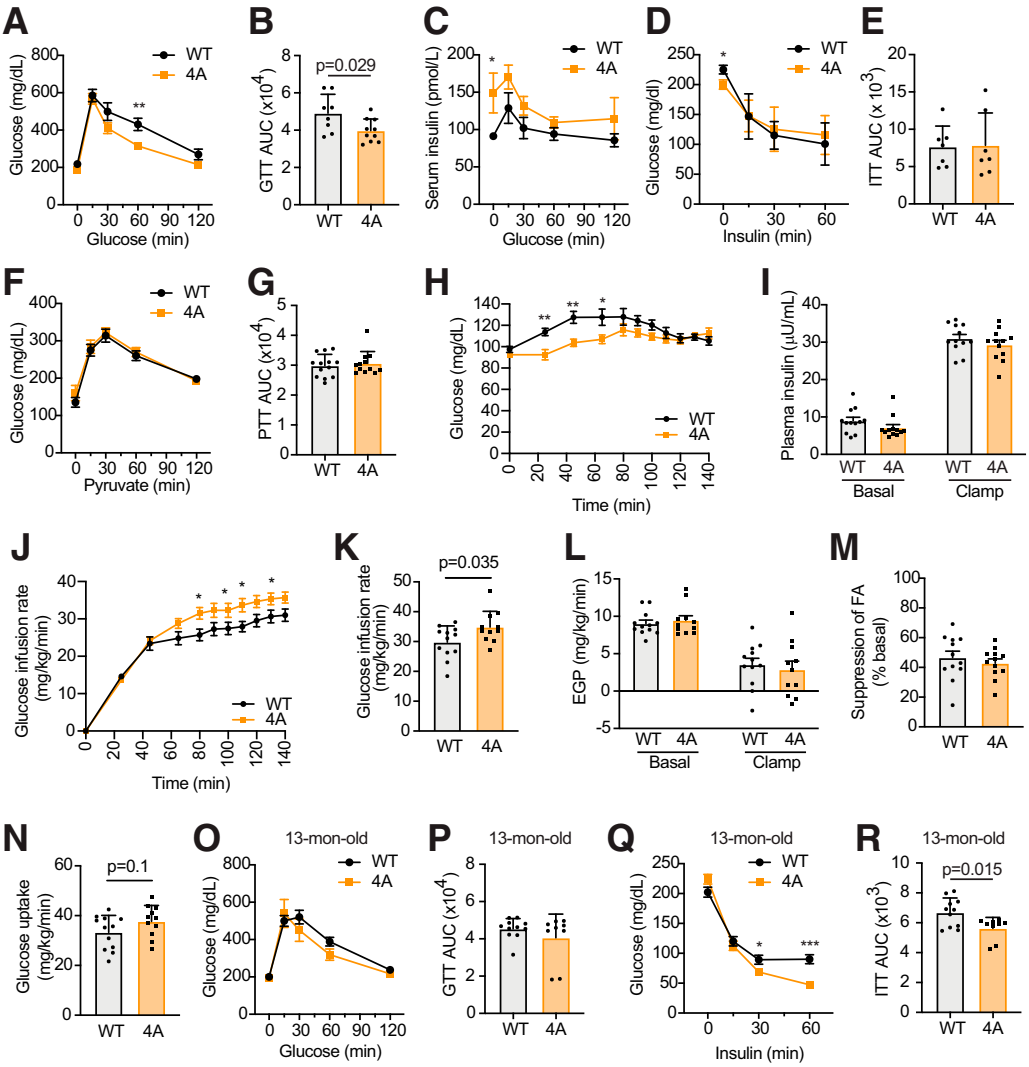

Figure 4—Metabolic phenotypes of IR-4A mice under normal chow conditions. *A*: Glucose tolerance test (GTT) in 2- to 3-month-old male mice. Mean ± SEM. WT, *N* = 8; IR-4A, *N* = 10. Significance calculated with two-tailed Student *t* test; $^{**}P < 0.01$. *B*: Glucose area under the curve (AUC) during glucose tolerance test in *A*. Mean ± SD. Significance calculated with two-tailed Student *t* test. *C*: Serum insulin levels during glucose tolerance test. Mean ± SEM. WT, *N* = 8; IR-4A, *N* = 6. Significance calculated with two-tailed Student *t* test; $^{*}P < 0.05$. *D*: ITT in 2- to 3-month-old male mice. Mean ± SEM. *N* = 7 mice each. Significance calculated with two-tailed Student *t* test; $^{*}P < 0.05$. *E*: Glucose area under the curve during ITT in *D*. *F*: PTT in 2- to 3-month-old male mice. Mean ± SEM. WT, *N* = 13; IR-4A, *N* = 12. *G*: Glucose area under the curve during PTT in *F*. *H–N*: Male IR-4A or WT littermate mice fed normal chow were fasted 14 h before hyperinsulinemic-euglycemic clamp studies. WT, *N* = 12; IR-4A, *N* = 11. *H*: Time course of plasma glucose required to achieve and maintain euglycemia. Mean ± SEM. Significance calculated with two-tailed Student *t* test. $^{*}P < 0.05$; $^{**}P < 0.01$. *I*: Plasma insulin concentrations during clamp studies. Mean ± SD. *J*: Time course of glucose infusion rates required to achieve and maintain euglycemia. Mean ± SEM. Significance calculated with two-tailed Student *t* test. $^{*}P < 0.05$. *K*: Steady-state glucose infusion rates during the clamp. Mean ± SD. Significance calculated with two-tailed Student *t* test. *L*: EGP during the basal period and the steady-state period of the clamp. Mean ± SEM. *M*: Whole-body FA suppression during the clamp. Mean ± SEM. *N*: Peripheral glucose uptake during the steady-state period of the clamp. Mean ± SD. *O*: Glucose tolerance test in 13-month-old male mice. Mean ± SEM. WT, *N* = 11; IR-4A, *N* = 9. *P*: Glucose area under the curve during glucose tolerance test in *O*. Mean ± SD. *Q*: ITT in 13-month-old male mice. Mean ± SEM. WT, *N* = 11; IR-4A, *N* = 9. Significance calculated with two-tailed Student *t* test; $^{*}P < 0.05$; $^{***}P < 0.001$. *R*: Glucose area under the curve during ITT in *Q*. Mean ± SD. Significance calculated with two-tailed Student *t* test. 4A, IR-4A; mon, month.

condensed to form ketone bodies. In addition, the energy released in this β-oxidation process is used by the liver for gluconeogenesis. Therefore, lipolysis in adipose tissues is essential for energy homeostasis during fasting.

To determine the role of the IR-MAD2 interaction in response to nutrient deprivation, we monitored the metabolic parameters of mice in fasting and refeeding conditions. In both fasting and random feeding conditions, IR-4A mice did not significantly differ from WT mice in body weight, liver mass, spleen mass, heart mass, kidney mass, or brown adipose tissue mass (Fig. 6*A* and Supplementary Fig. 4*A* and *B*). By H-E stain, IR-4A liver appears normal (Supplementary

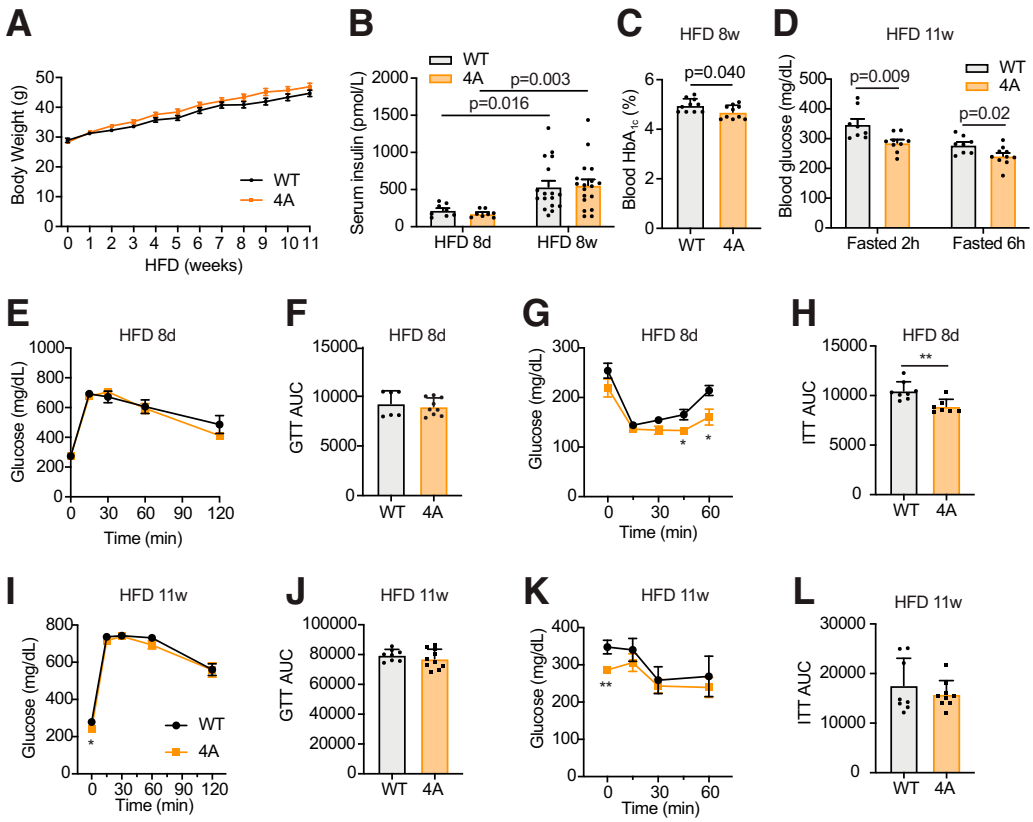

Figure 5—Metabolic phenotypes of IR-4A mice under HFD conditions. *A*: Body weight curves of mice fed HFD for 11 weeks. Mean ± SEM. WT, *N* = 14; IR-4A, *N* = 19. B: Serum insulin level in male mice fasted 6 h fed HFD for 8 days (8d) or 8 weeks (8w). Mean ± SD. WT fed HFD for 8 days, *N* = 8; IR-4A fed HFD for 8 days, *N* = 8; WT fed HFD for 8 weeks, *N* = 17; IR-4A fed HFD for 8 weeks, *N* = 18. Significance calculated with two-tailed Student *t* test. *C*: Blood HbA_{1c} level in male mice fed HFD for 8 weeks in random feeding conditions. Mean ± SD. *N* = 10 mice each. Significance calculated with two-tailed Student *t* test. *D*: Blood glucose level in mice fed HFD for 11 weeks (11w). Mean ± SEM. WT fasted 2 h, *N* = 8; IR-4A fasted 6 h, *N* = 9; WT fasted 6 h, *N* = 8; IR-4A fasted 6 h, *N* = 10. Significance calculated with two-tailed Student *t* test. *E*: Glucose tolerance test (GTT) in male mice fed HFD for 8 days. Mean ± SEM. WT, *N* = 6; IR-4A, *N* = 9. *F*: Glucose area under the curve (AUC) during glucose tolerance test in *E*. Mean ± SD. *G*: ITT in male mice fed HFD for 8 days. Mean ± SEM. WT, *N* = 8; IR-4A, *N* = 7. Significance calculated with two-tailed Student *t* test. *$P < 0.05$. *H*: Glucose AUC during ITT in *G*. Mean ± SD. Significance calculated with two-tailed Student *t* test. **$P < 0.01$. *I*: Glucose tolerance test in male mice fed HFD for 11 weeks. Mean ± SEM. WT, *N* = 8; IR-4A, *N* = 10. Significance calculated with two-tailed Student *t* test. *$P < 0.05$. *J*: Glucose area under the curve during glucose tolerance test in *I*. Mean ± SD. *K*: ITT in male mice fed HFD for 11 weeks. Mean ± SEM. WT, *N* = 8; IR-4A, *N* = 9. Significance calculated with two-tailed Student *t* test. **$P < 0.01$. *L*: Glucose area under the curve during ITT in *K*. Mean ± SD. 4A, IR-4A.

Fig. 4*C*). However, despite no observable difference in hepatic glycogen levels between WT and IR-4A mice (Supplementary Fig. 4*D*), there was a substantial increase in Oil red O staining and hepatic TG contents in IR-4A mice after a 20-h fast (Fig. 6*B* and *C*). Feeding decreased and similarly restored hepatic TG content in both WT and IR-4A mice (Fig. 6*B* and *C*). We found no difference in circulating TG levels during fasting and refeeding conditions (Fig. 6*D*), while the serum FA level was increased in fasted IR-4A mice (Fig. 6*E*). Strikingly, white adipose tissue (WAT) mass of IR-4A mice was significantly increased, especially eWAT, which increased by ∼30% in the fed state and by ∼40% after fasting for 20 h (Fig. 6*A* and Supplementary Fig. 4*B*). IR-4A mice had larger adipocyte size in fat deposits examined after a 20-h fast (Fig. 6*F* and *G*). Furthermore, IR-4A WAT showed a slight increase in hormone-sensitive lipase (HSL) phosphorylation (Supplementary Fig. 4*E* and *F*), suggesting that TG hydrolysis is potentially enhanced. These data suggest a role of the IR-MAD2 interaction in lipid metabolism during fasting.

We examined genes involved in lipid regulation in liver and eWAT of WT and IR-4A mice during 20 h of fasting. Although IR-4A livers have elevated TG content, lipogenesis genes including *Srebp1* and *Scd1* were decreased, whereas TG synthesis (*Dgat1*) and lipid transport (*Cd36* and *Slc27a2*) genes were increased in IR-4A livers (Fig. 6*H*). A β-oxidation regulator, *Cpt1*, was expressed normally. In eWAT of IR-4A mice, expression of genes involved in lipogenesis (*Acc1* and *Fasn*), lipid transport (*Cd36*, *Lpl*, and *Fabp4*), and lipolysis (*Lipe* and *Plin1*) was increased; however, expression of genes that control TG synthesis (*Agpat3*, *Dgat1*, and *Dgat2*) was normal (Fig. 6*I*). Collectively, these results suggest that disruption of the IR-MAD2 interaction may enhance lipogenesis, lipid transport, and lipolysis in the adipose tissue during fasting, thus

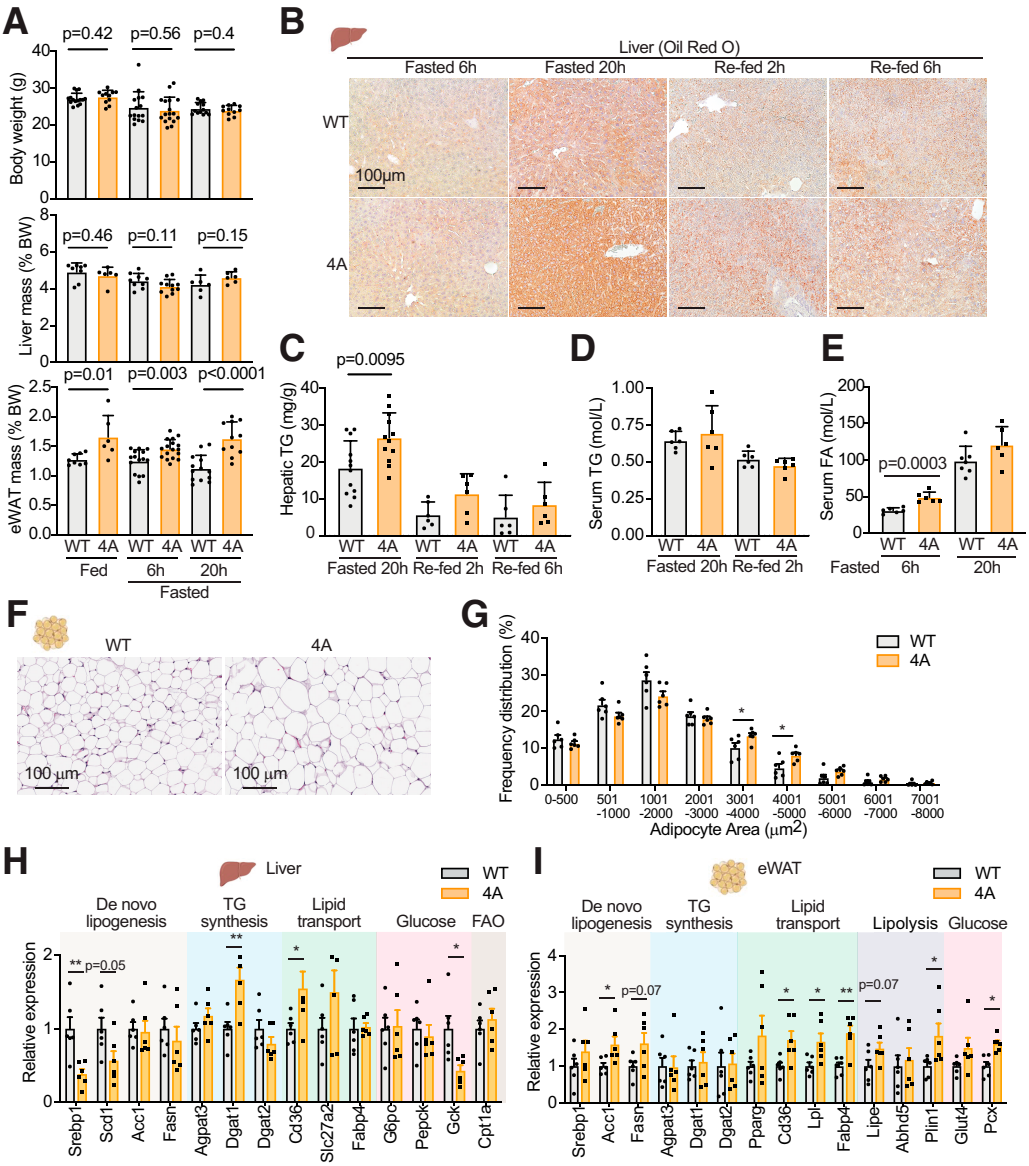

Figure 6—IR-MAD2 controls energy homeostasis. *A*: Body weight, liver mass, and eWAT mass of 2- to 3-month-old male mice fed normal chow diet. Mean ± SD. For body weight and eWAT, WT, fed, $N = 8$; IR-4A, fed, $N = 6$; WT, fasted 6 h, $N = 15$; IR-4A, fasted 6 h, $N = 17$; WT, fasted 20 h, $N = 6$; IR-4A, fasted 20 h, $N = 6$. For liver mass, WT, fed, $N = 8$; IR-4A, fed, $N = 6$; WT, fasted 6 h, $N = 9$; IR-4A, fasted 6 h, $N = 11$; WT, fasted 20 h, $N = 6$; IR-4A, fasted 20 h, $N = 6$. Significance calculated with two-tailed Student *t* test. *B*: Representative images of Oil red O staining of the liver sections.*C*: Hepatic contents of triglycerols (TG). Mean ± SEM. WT, fasted 20 h, $N = 12$; IR-4A, fasted 20 h, $N = 12$; IR WT, refed 2 h, $N = 6$; IR-4A, refed 2 h, $N = 6$; IR WT, refed 6 h, $N = 6$; IR-4A, refed 6 h, $N = 6$. Significance calculated with two-tailed Student *t* test. *D*: Serum content of TG. Mean ± SD. $N = 6$ mice each. *E*: Serum content of fatty acid (FA). Mean ± SD. WT, fasted 6 h, $N = 6$; IR-4A, fasted 6 h, $N = 6$; WT, fasted 20 h, $N = 7$; IR-4A, fasted 20 h, $N = 6$. Significance calculated with two-tailed Student *t* test. *F*: Representative images of H-E of WAT from 2- to 3-month-old mice fed normal chow diet. *G*: Adipocyte size distribution. Mean ± SEM. $N = 6$ mice each. WT, $N = 19{,}930$ cells; IR-4A, $N = 22{,}439$ cells. *H*: Relative levels of hepatic mRNAs for genes involved in lipid and glucose metabolism (fasted 20 h). Mean ± SEM. $N = 6$ mice each. Significance calculated with two-tailed Student *t* test. $^*P < 0.05$; $^{**}P < 0.01$; FAO, fatty acid oxidation. *I*: Relative levels of WAT mRNAs for genes involved in lipid and glucose metabolism (fasted 20 h). Mean ± SEM. $N = 6$ mice each. Significance calculated with two-tailed Student *t* test. $^*P < 0.05$; $^{**}P < 0.01$. 4A, IR-4A; BW, body weight.

increasing circulating FA and promoting hepatic fat accumulation.

To investigate the metabolic effect of the IR-MAD2 interaction in adipose tissues, we examined the potency of adipocyte differentiation and insulin-mediated suppression of lipolysis in vitro (Supplementary Fig. 5*A* and *B*in vivo results, no defects were observed in the adipogenic capacity of IR-4A mouse embryonic fibroblasts. Insulin significantly inhibited isoproterenol-stimulated lipolysis in both WT and IR-4A mouse embryonic fibroblast–derived adipocytes (Supplementary Fig. 5*C*). A similar result was obtained in the ex vivo adipose tissue culture (Supplementary Fig. 5*D*), indicating that increased FA release from IR-4A adipose tissues is not associated with the defects in differentiation or insulin sensitivity.

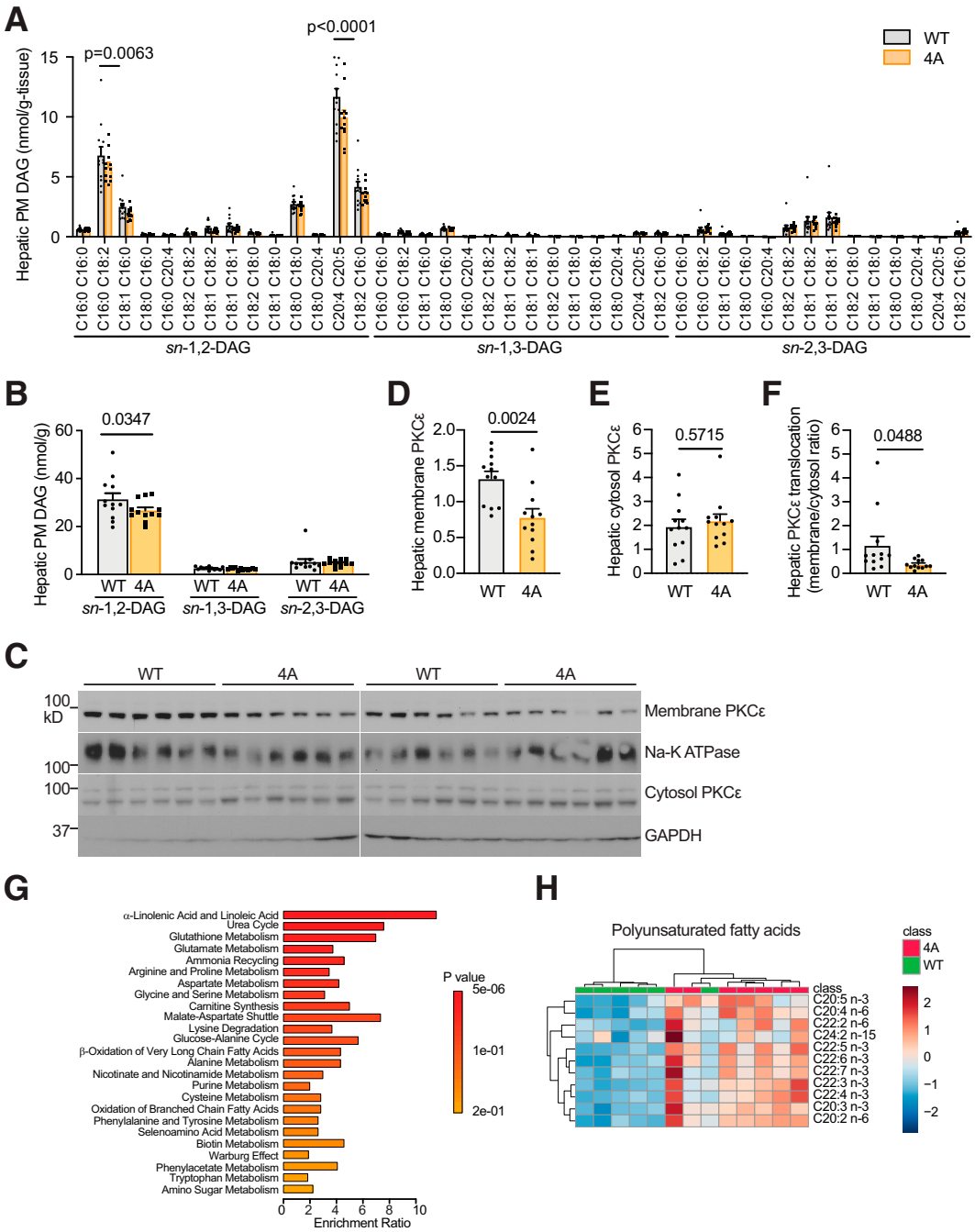

Figure 7—IR-MAD2 controls levels of hepatic PM *sn*-1,2-DAG and plasma PUFA. *A* and *B*: The different components (*A*) and total (*B*) hepatic PM DAG content. Two-month-old male mice fed normal chow diet were fasted for 6 h. Mean ± SEM. *N* = 12 mice each. Significance calculated with two-tailed Student *t* test. *C*: Hepatic PKCε protein content measured with Western blot. Two-month-old male mice fed normal chow diet were fasted for 6 h. *D*: Quantification of the Western blot data shown in hepatic membrane PKCε (*C*). Mean ± SEM. *N* = 12 mice each. Significance calculated with two-tailed Student *t* test. *E*: Quantification of the Western blot data shown in hepatic cytosol PKCε (*C*). Mean ± SEM. *N* = 12 mice each. Significance calculated with two-tailed Student *t* test. *F*: Hepatic PKCε translocation from cytosol to membrane. Mean ± SEM. *N* = 12 mice each. Significance calculated with two-tailed Student *t* test. *G*: Metabolite set enrichment analysis of plasma samples of IR-4A mice compared with WT. WT, *N* = 6; IR-4A, *N* = 7. *H*: Heat map of identified PUFA in plasma samples of WT and IR-4A mice. 4A, IR-4A.

The Function of IR-MAD2 in Insulin Transcytosis

IR-mediated transcytosis determines insulin sensitivity in peripheral tissues such as adipose tissue and muscle with a continuous capillary system (36,37). We tested whether disruption of the IR-MAD2 interaction inhibits the IR-mediated uptake and release of insulin in endothelial cells. We analyzed insulin fate in the $CD31^{+}$ primary endothelial cells isolated from WT and IR-4A eWAT, and L6 myoblasts (Supplementary Fig. 6*A* and *B*). The insulin taken up by L6 cells gradually disappeared, and there was no detectable

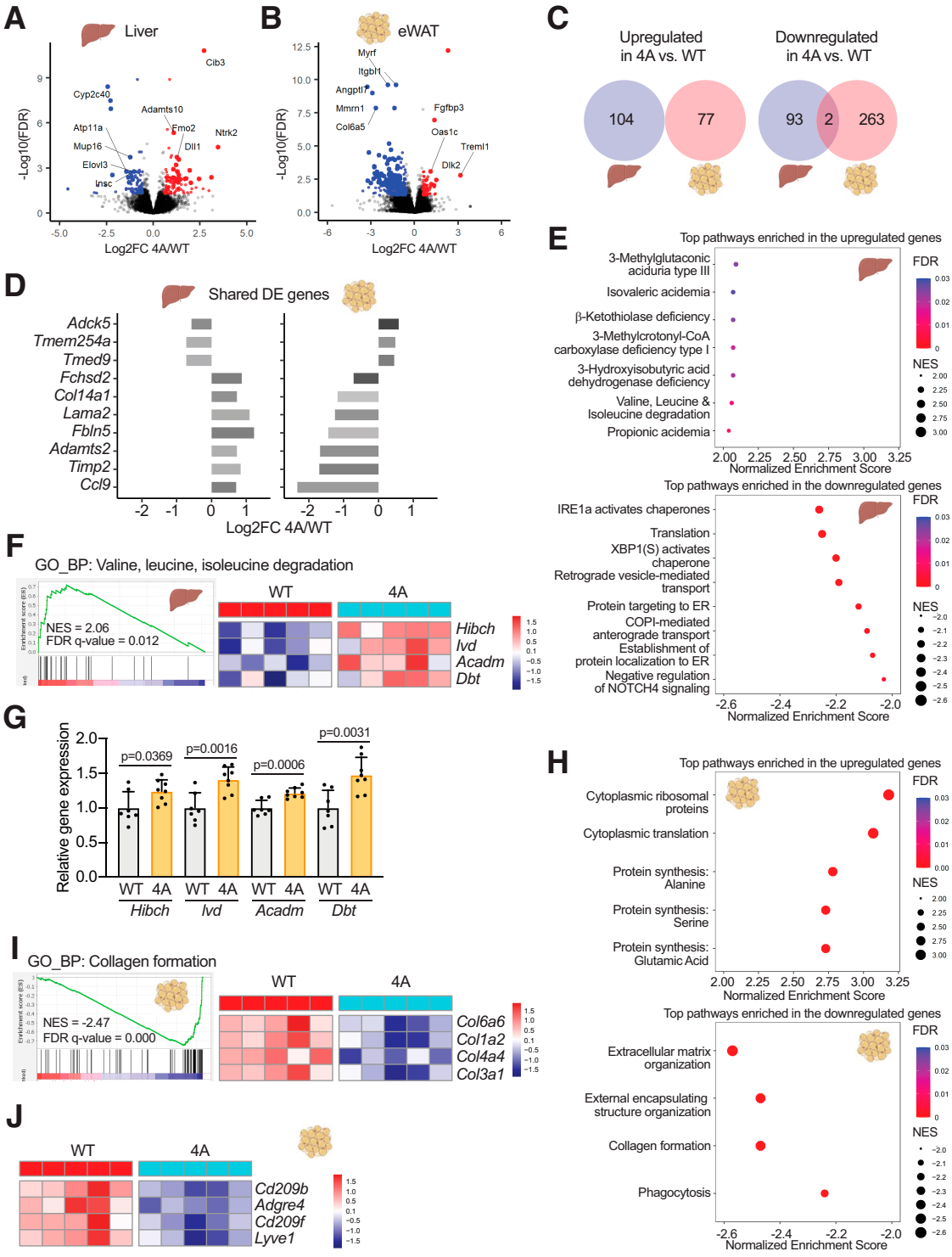

Figure 8—Gene expression changes in the liver and eWAT of IR-4A mice. *A* and *B*: Volcano plots to visualize the DE genes in liver (*A*) and eWAT (*B*). Genes with a false discovery rate (FDR)-adjusted *P* value <0.05 and a Log2 fold change (FC) >0.58 or less than -0.58 are considered DE. Log2 fold change is plotted against the $-$Log10(FDR) for each gene, where FDR is false discovery rate. Blue dots represent DE genes that are downregulated and red dots represent DE genes that are upregulated in IR-4A mice. $N = 5$ mice each. *C*: Venn diagrams of DE genes in *A* and *B*. *D*: Shared DE genes with opposite directionality of expression between liver and eWAT. *E*: Representative gene sets that show enrichment in the upregulated (upper panel) and downregulated (lower panel) genes in IR-4A mice by gene set enrichment analysis with liver transcriptomics data. *F*: Upper panel: enrichment plot for the valine, leucine, and isoleucine degradation pathway as shown in *E* visualizing the positions of gene set members on the rank-ordered list. Lower panel: visualization of the expression of leading-edge genes in the pathway using a heat map. *G*: Relative levels of hepatic mRNAs for genes involved in valine, leucine, and isoleucine metabolism, analyzed with quantitative PCR. WT, $N = 7$; IR-4A, $N = 8$. Significance calculated with two-tailed Student *t* test. *H*: Representative gene sets that show enrichment in the upregulated (upper panel) and downregulated (lower panel) genes in IR-4A mice by gene set

insulin in the medium. In contrast, the insulin taken by $CD31^+$ primary endothelial cells decreased over time and was released in the supernatant, indicating insulin release from endothelial cells. In this condition, we did not observe significant differences between WT and IR-4A primary endothelial cells. Note that due to the detection limit of this assay, we could not further reduce the insulin concentration in the pulse to near-physiological concentrations.

Brain has a blood-brain barrier, limiting access of circulating insulin (38). Insulin signaling is delayed in brains of endothelial IR KO mice because insulin transcytosis is inhibited (39). Although IR levels were increased in the IR-4A hypothalamus, pIR and pAKT levels did not differ (Supplementary Fig. 6*C*). These data suggest that the disruption of the IR-MAD2 interaction did not affect the transcytosis of insulin in supraphysiological conditions.

The Function of IR-MAD2 in PKCε-Mediated Hepatic Insulin Resistance

Hepatic PKCε activation is required for the induction of lipid-induced hepatic insulin resistance (40,41). PM *sn*-1,2-DAGs in the liver activate PKCε, which then phosphorylates IR T^{1160} (T^{1150} in mouse), resulting in reduced IR kinase activity and hepatic insulin resistance (25,42). To examine the role of the IR-MAD2 interaction in hepatic regulation of PKCε, we examined the total DAG levels in PM using differential centrifugation and liquid chromatography–tandem mass spectrometry method (25). Disruption of the IR-MAD2 interaction reduced the *sn*-1,2-DAG level in the hepatic PM (Fig. 7*A* and *B*). In contrast, there were no discernible differences observed for *sn*-2,3-DAG and *sn*-1,3-DAG in the hepatic PM. Consistent with the reduction of PM *sn*-1,2-DAG in IR-4A liver, IR-4A mutation reduced the amount of membrane PKCε content in the liver with ∼30% lower translocation without altering cytosol PKCε content (Fig. 7*C*–*F*). Despite marginally prolonged and enhanced hepatic insulin signaling (Fig. 2), improved glucose clearance (Fig. 4*A*, *J*, and *K*), and decreased *sn*-1,2-DAG contents in the hepatic PM (Fig. 7*A* and *B*), IR-4A mutation did not affect EGP during the clamp (Fig. 4*L*). Previous studies demonstrating a relatively minor role for direct hepatic insulin signaling in regulating hepatic glucose production, in rodents without severe hepatic steatosis (43), might partly explain this inconsistency.

Functions of IR-MAD2 in the Metabolomic and Transcriptomic Profiles

Because disruption of the IR-MAD2 interaction altered PM *sn*-1,2-DAG levels and fat accumulation in the liver during fasting, we assessed which metabolic pathways were affected under these circumstances. We first used metabolomics analysis in the plasma of WT and IR-4A mice fasted for 6 h. Heat map analysis with hierarchical clustering demonstrated that plasma metabolites in IR-4A mice clearly separated from those in WT mice (Supplementary Fig. 7*A*), implying their distinct metabolic phenotype in comparison with WT mice. Using a metabolite set enrichment analysis (44) on plasma metabolomics data, we found that the most affected metabolite sets were those related to linolenic acid and linoleic acid pathways (Fig. 7*G*). Consistent with these findings, linolenic acid, arachidonic acid, and docosahexaenoic acid levels were altered in IR-4A mice (Supplementary Fig. 7*A*). Further analysis demonstrated that plasma levels of polyunsaturated FA (PUFA) were increased by IR-4A mutation (Fig. 7*H*). In contrast, the levels of saturated FA, monounsaturated FA, and FA derivatives in the plasma from IR-4A mice did not form a distinct cluster away from that of WT mice (Supplementary Fig. 7*B*).

We next assessed transcriptomic profile in the liver and eWAT from WT and IR-4A mice after 6 h fasting using RNA sequencing. There is a distinction between differentially expressed (DE) genes with minimal overlap (Fig. 8*A*–*C*) and several shared DE genes with opposite fold changes (Fig. 8*D*), suggesting that IR-4A mice displayed distinct effects on transcriptomic profiles between liver and eWAT. The upregulated genes in IR-4A liver showed a significant enrichment for genes in pathways regulating the catabolism of leucine and valine, including *Hibch*, *Ivd*, *Acadm*, and *Dbt*, that contribute to FA synthesis (Fig. 8*E*–*G*). The downregulated genes in IR-4A liver showed a significant enrichment for genes in pathways regulating protein localization and targeting to the endoplasmic reticulum (Fig. 8*E*). An analysis of plasma metabolomics revealed that the levels of the branched chain amino acids leucine and valine were not altered in IR-4A mice (Supplementary Fig. 7*C*). These data suggest that although RNA-sequencing data suggest a potential increase in the catabolism of leucine and valine in IR-4A liver, liver leucine and valine catabolism may not regulate or be influenced by circulating levels of leucine and valine (Fig. 8*E*–*G*).

In eWAT, the upregulated genes in IR-4A mice showed an enrichment for genes in pathways regulating protein synthesis and translation (Fig. 8*H*). The downregulated genes in IR-4A eWAT showed an enrichment for genes in pathways regulating collagen formation and extracellular matrix organization (e.g., *Col6a6*, *Col1a2*, *Col4a4*, and *Col3a1*) (Fig. 8*H* and *I*). We also observed significantly lower expression of several macrophage markers, including *Cd209b*, *Adgre4*, *Cd209f*, and *Lyve1*, in IR-4A eWAT (Fig. 8*J*). Given the fact that PUFAs have anti-inflammatory effects (45,46), increased serum PUFA levels in IR-4A mice (Fig. 7*H*) may regulate macrophages population or gene expression in the eWAT. Altogether, the data support a profound change in the whole-body metabolism of IR-4A mice and the distinct effects on the transcriptomic profiles between the liver and adipose tissue.

enrichment analysis with eWAT transcriptomics data. *I*: Upper panel: enrichment plot for the collagen formation pathway as shown in *H* visualizing the positions of gene set members on the rank-ordered list. Lower panel: visualization of the expression of leading-edge genes in the pathway using a heat map. *J*: Heat map of macrophage marker genes downregulated in the eWAT of IR-4A mice. 4A, IR-4A; ER, endoplasmic reticulum; NES, normalized enrichment score; GO_BP, Gene Ontology_Biological Process.

DISCUSSION

In this study, we have determined the physiological function of IR-MAD2 interaction during insulin signaling and metabolic homeostasis. Specifically, we find that disruption of the IR-MAD2 interaction delays insulin-dependent in vivo. This genetic attenuation of IR endocytosis slightly enhances and prolongs insulin signaling through the PI3K-AKT pathway and does not appreciably affect the other branch of insulin signaling, the MAPK pathway. The elevated PI3K-AKT signaling in these mice may account for the improved insulin sensitivity when circulating insulin levels are similar. Alternatively, signaling events proximal to the PM are more effective in mediating metabolic regulation by insulin. At present, we do not know why signaling through the MAPK pathway is not enhanced in IR-4A hepatocytes. One possibility is that the IR-MAD2 interaction facilitates activation of the MAPK pathway by insulin.

in vivo when insulin levels are equal. We propose that increased levels of insulin and surface IR enhance insulin functions in the adipose tissues of IR-4A mice (Supplementary Fig. 8). Indeed, IR-4A mice exhibited enlarged WAT. We speculate that WAT of IR-4A mice may release more FA under nutrient-deficient conditions because they store more fat in the WAT during feeding. This partly explains why IR-4A mice exhibited elevated levels of circulating FA and hepatic TG during long-term fasting.

On the other hand, IR-4A mice exhibited increased glucose counterregulatory factors such as glucagon, thus affecting glucose control (Supplementary Fig. 8). Therefore, early during HFD feeding, disruption of the IR-MAD2 interaction delays insulin resistance, but at a later stage, the compensatory effect and the comparability of serum insulin levels result in diet-induced metabolic complications in IR-4A mice. The underlying mechanism of hyperglucagonemia in IR-4A mice remains unclear. One possibility is that mild hypoglycemia in IR-4A mice causes glucagon secretion. However, IR-4A mice do not reach the hypoglycemic threshold that induces glucagon secretion (47), suggesting additional regulation. Insulin inhibits glucagon release by promoting somatostatin secretion (48), and glucagon stimulates insulin secretion through glucagon receptor and glucagon-like peptide 1 receptor (49). In addition, the sympathetic and parasympathetic branches of autonomic nervous systems control insulin and glucagon secretion (50). It will be intriguing to determine whether or how the IR-MAD2 controls the activation of the counterregulatory factors in islet and nervous system.

Although we did not observe defects in insulin uptake and release in the endothelial cells and insulin signaling in the brain of IR-4A mice, we cannot rule out the possibility that MAD2 binding deficiency diminishes insulin transcytosis and alters local insulin levels because all experiments were conducted under supraphysiological insulin concentrations. While our whole-body knock-in IR-4A mouse is a powerful system for understanding the systemic function of IR-MAD2, the relative contributions of different processes in different tissues to the global phenotype are difficult to ascertain. Future experiments using tissue-specific conditional knock-in IR-4A mouse are needed to further define the tissue-specific functions of this interaction.

Hyperinsulinemia is associated with insulin resistance, although the cause-effect relationship remains obscure. IR-mediated insulin uptake and degradation are essential mechanisms for insulin clearance. Therefore, the rate of IR endocytosis and the extent of surface IR levels are directly related to circulating insulin levels. Previous studies with use of IR or CEACAM1 KO mice support the idea that the impaired insulin clearance causes insulin resistance. Conversely, IR endocytosis defects caused by hepatic EPHB4 or SHP2 inhibition reduce insulin resistance and improve glucose tolerance. $p31^{comet}$-deficient mice exhibit reduced basal surface IR levels and defective insulin signaling, while BUBR1 deficiency enhances insulin sensitivity and rescues the metabolic defects of $p31^{comet}$-deficient mice (22in vivo and establish a physiological function of IR trafficking in insulin and glucose homeostasis.

Acknowledgments. The authors thank Dr. Caiying Guo and colleagues (HHMI's Janelia Research Campus) for generating the IR-4A mice, Dr. Sei Higuchi for technical assistance, and Drs. Joseph Goldstein, David Mangelsdorf, and Li Qiang for helpful discussion. The authors are grateful to the Animal Resource Center at Columbia University for assistance with mouse maintenance and the Molecular Pathology Core for assistance with tissue processing and sectioning.

Funding. The authors' research work has received funding from the National Institutes of Health (NIH) (R01DK132361 to E.C.; R00HL130574 and R01HL151611 to H.Z.; R01HL125649 and R01DK115825 to R.A.H.; P30DK063608 to E.C., R.A.H., and D.A.; UL1TR001873 to E.C. and H.Z.; and UC2DK134901, P30DK045735, and R01DK133143 to G.I.S.), Alice Bohmfalk Charitable Trust (to E.C.), American Lung Association (IA-828202), American Cancer Society (RSG-21-153-01-CCB) (to J.K.), and American Heart Association (postdoctoral fellowship 20POST35130003 and Career Development Award 23CDA1052177 to F.L.). The authors acknowledge the NIH funding sources to the Biomarkers Core Laboratory at the Irving Institute for Clinical and Translational Research, home to Columbia University's Clinical and Translational Science Award (UL1TR001873); the Genomics and High Throughput Screening Shared Resource (NIH/National Cancer Institute Cancer Center Support Grant P30CA013696); and the Columbia University Digestive and Liver Diseases Research Center (P30DK132710).

The content in this manuscript is solely the responsibility of the authors and does not necessarily represent the official views of the NIH.

Duality of Interest. No potential conflicts of interest relevant to this article were reported.

Author Contributions. J.P. designed and performed experiments and analyzed data. C.H. measured the body weight of a mouse on a high-fat diet and analyzed data. B.H., T.L., R.G., and A.N. performed hyperinsulinemic-euglycemic clamp study and PKCε analysis. F.L. and H.Z. performed transcriptomic profile analysis. J.K. performed metabolomic profile analysis. R.A.H. and D.A. provided suggestions. G.I.S. supervised hyperinsulinemic-euglycemic clamp study and PKCε analysis and provided suggestions. H.Y. supervised the project and provided suggestions. E.C. supervised the project, performed experiments, and analyzed data. J.P. and E.C. wrote the manuscript with input from other authors. E.C. is the guarantor of this work and, as such, had full access to all the data in the study and takes responsibility for the integrity of the data and the accuracy of the data analysis.

References

1. Haeusler RA, McGraw TE, Accili D. Biochemical and cellular properties of insulin receptor signalling. Nat Rev Mol Cell Biol 2018;19:31–44

2. Li J, Park J, Mayer JP, et al. Synergistic activation of the insulin receptor via two distinct sites. Nat Struct Mol Biol 2022;29:357–368
3. Uchikawa E, Choi E, Shang G, Yu H, Bai XC. Activation mechanism of the insulin receptor revealed by cryo-EM structure of the fully liganded receptor-ligand complex. eLife 2019;8:e48630
4. Boucher J, Kleinridders A, Kahn CR. Insulin receptor signaling in normal and insulin-resistant states. Cold Spring Harb Perspect Biol 2014;6:a009191
5. Menting JG, Whittaker J, Margetts MB, et al. How insulin engages its primary binding site on the insulin receptor. Nature 2013;493:241–245
6. Choi E, Bai XC. The activation mechanism of the insulin receptor: a structural perspective. Annu Rev Biochem 2023;92:247–272
7. Cinti S, Eberbach S, Castellucci M, Accili D. Lack of insulin receptors affects the formation of white adipose tissue in mice. A morphometric and ultrastructural analysis. Diabetologia 1998;41:171–177
8. Petersen MC, Shulman GI. Mechanisms of insulin action and insulin resistance. Physiol Rev 2018;98:2133–2223
9. Gallagher EJ, LeRoith D. The proliferating role of insulin and insulin-like growth factors in cancer. Trends Endocrinol Metab 2010;21:610–618
10. Hall C, Yu H, Choi E. Insulin receptor endocytosis in the pathophysiology of insulin resistance. Exp Mol Med 2020;52:911–920
11. Chen Y, Huang L, Qi X, Chen C. Insulin receptor trafficking: consequences for insulin sensitivity and diabetes. Int J Mol Sci 2019;20:5007
12. Iraburu MJ, Garner T, Montiel-Duarte C. Revising endosomal trafficking under insulin receptor activation. Int J Mol Sci 2021;22:6978
13. Wu J, Park SH, Choi E. The insulin receptor endocytosis. Prog Mol Biol Transl Sci 2023;194:79–107
14. Saltiel AR. Insulin signaling in health and disease. J Clin Invest 2021; 131:e142241
15. Najjar SM, Caprio S, Gastaldelli A. Insulin clearance in health and disease. Annu Rev Physiol 2023;85:363–381
16. Bergman RN, Kabir M, Ader M. The physiology of insulin clearance. Int J Mol Sci 2022;23:1826
17. Ghadieh HE, Russo L, Muturi HT, et al. Hyperinsulinemia drives hepatic insulin resistance in male mice with liver-specific Ceacam1 deletion independently of lipolysis. Metabolism 2019;93:33–43
18. Michael MD, Kulkarni RN, Postic C, et al. Loss of insulin signaling in hepatocytes leads to severe insulin resistance and progressive hepatic dysfunction. Mol Cell 2000;6:87–97
19. Poy MN, Yang Y, Rezaei K, et al. CEACAM1 regulates insulin clearance in liver. Nat Genet 2002;30:270–276
20. Liu X, Wang K, Hou S, et al. Insulin induces insulin receptor degradation in the liver through EphB4. Nat Metab 2022;4:1202–1213
21. Ansarullah JC, Jain C, Far FF, et al. Inceptor counteracts insulin signalling in β-cells to control glycaemia. Nature 2021;590:326–331
22. Choi E, Zhang X, Xing C, Yu H. Mitotic checkpoint regulators control insulin signaling and metabolic homeostasis. Cell 2016;166:567–581
23. Choi E, Kikuchi S, Gao H, et al. Mitotic regulators and the SHP2-MAPK pathway promote IR endocytosis and feedback regulation of insulin signaling. Nat Commun 2019;10:1473
24. Park J, Li J, Mayer JP, et al. Activation of the insulin receptor by an insulin mimetic peptide. Nat Commun 2022;13:5594
25. Lyu K, Zhang Y, Zhang D, et al. A membrane-bound diacylglycerol species induces PKCε-mediated hepatic insulin resistance. Cell Metab 2020; 32:654–664.e5
26. Goh LK, Sorkin A. Endocytosis of receptor tyrosine kinases. Cold Spring Harb Perspect Biol 2013;5:a017459
27. Russo L, Muturi HT, Ghadieh HE, et al. Liver-specific reconstitution of CEACAM1 reverses the metabolic abnormalities caused by its global deletion in male mice. Diabetologia 2017;60:2463–2474
28. Mullins GR, Wang L, Raje V, et al. Catecholamine-induced lipolysis causes mTOR complex dissociation and inhibits glucose uptake in adipocytes. Proc Natl Acad Sci U S A 2014;111:17450–17455
29. Deibert DC, DeFronzo RA. Epinephrine-induced insulin resistance in man. J Clin Invest 1980;65:717–721
30. Møller N, Jørgensen JO. Effects of growth hormone on glucose, lipid, and protein metabolism in human subjects. Endocr Rev 2009;30:152–177
31. Minaker KL, Rowe JW, Tonino R, Pallotta JA. Influence of age on clearance of insulin in man. Diabetes 1982;31:851–855
32. Fink RI, Revers RR, Kolterman OG, Olefsky JM. The metabolic clearance of insulin and the feedback inhibition of insulin secretion are altered with aging. Diabetes 1985;34:275–280
33. McGuire EA, Tobin JD, Berman M, Andres R. Kinetics of native insulin in diabetic, obese, and aged men. Diabetes 1979;28:110–120
34. Geisler CE, Hepler C, Higgins MR, Renquist BJ. Hepatic adaptations to maintain metabolic homeostasis in response to fasting and refeeding in mice. Nutr Metab (Lond) 2016;13:62
35. Rodgers JT, Puigserver P. Fasting-dependent glucose and lipid metabolic response through hepatic sirtuin 1. Proc Natl Acad Sci U S A 2007;104:12861–12866
36. Lee WL, Klip A. Endothelial transcytosis of insulin: does it contribute to insulin resistance? Physiology (Bethesda) 2016;31:336–345
37. Bergman RN, Iyer MS. Indirect regulation of endogenous glucose production by insulin: the single gateway hypothesis revisited. Diabetes 2017;66:1742–1747
38. Abbott NJ, Patabendige AA, Dolman DE, Yusof SR, Begley DJ. Structure and function of the blood-brain barrier. Neurobiol Dis 2010;37:13–25
39. Konishi M, Sakaguchi M, Lockhart SM, et al. Endothelial insulin receptors differentially control insulin signaling kinetics in peripheral tissues and brain of mice. Proc Natl Acad Sci U S A 2017;114:E8478–E8487
40. Samuel VT, Shulman GI. Nonalcoholic fatty liver disease as a nexus of metabolic and hepatic diseases. Cell Metab 2018;27:22–41
41. Magkos F, Su X, Bradley D, et al. Intrahepatic diacylglycerol content is associated with hepatic insulin resistance in obese subjects. Gastroenterology 2012;142:1444–6.e2
42. Petersen MC, Madiraju AK, Gassaway BM, et al. Insulin receptor Thr1160 phosphorylation mediates lipid-induced hepatic insulin resistance. J Clin Invest 2016;126:4361–4371
43. Samuel VT, Shulman GI. The pathogenesis of insulin resistance: integrating signaling pathways and substrate flux. J Clin Invest 2016;126:12–22
44. Xia J, Wishart DS. MSEA: a web-based tool to identify biologically meaningful patterns in quantitative metabolomic data. Nucleic Acids Res 2010;38:W71-7
45. Calder PC. n-3 polyunsaturated fatty acids, inflammation, and inflammatory diseases. Am J Clin Nutr 2006;83(Suppl.):1505S–1519S
46. Yang Q, Vijayakumar A, Kahn BB. Metabolites as regulators of insulin sensitivity and metabolism. Nat Rev Mol Cell Biol 2018;19:654–672
47. Le Marchand SJ, Piston DW. Glucose suppression of glucagon secretion: metabolic and calcium responses from alpha-cells in intact mouse pancreatic islets. J Biol Chem 2010;285:14389–14398
48. Vergari E, Knudsen JG, Ramracheya R, et al. Insulin inhibits glucagon release by SGLT2-induced stimulation of somatostatin secretion. Nat Commun 2019;10:139
49. Svendsen B, Larsen O, Gabe MBN, et al. Insulin secretion depends on intra-islet glucagon signaling. Cell Rep 2018;25:1127–1134.e2
50. Thorens B. Brain glucose sensing and neural regulation of insulin and glucagon secretion. Diabetes Obes Metab 2011;13(Suppl. 1):82–88